Materials & Design 244 (2024) 113227

Contents lists available at ScienceDirect

Materials & Design

journal homepage: www.elsevier.com/locate/matdes

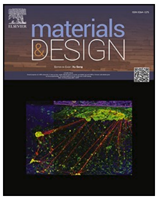

Numerical modelling of flexural performance of textile reinforced mortar strengthened concrete beams

Peng Cao [a], Liang Cao [a], Guoqing Chen [b], Zhengdong Zhi [c], Jianru Wang [d], Zhidan Yuan [e,*], Zhifei Tan [f,*]

[a] Faculty of Architecture, Civil and Transportation Engineering, Beijing University of Technology, Beijing 100124, China
[b] School of Architecture and Engineering, Northeast Electric Power University, Jilin 132012, China
[c] School of Civil Engineering, Yancheng Institute of Technology, Yancheng 224051, China
[d] Academy of Aerospace Solid Propulsion Technology, Xi'an 710025, China
[e] Yancheng Maolei Information Science & Technology, Co., Ltd, Yancheng 224001 China
[f] Department of Civil and Environmental Engineering, The Hong Kong Polytechnic University, Hong Kong, China

ARTICLE INFO

Keywords:
Textile reinforced mortar
Concrete beam
Finite element model
Flexural performance

ABSTRACT

In recent years, the application of textile reinforced mortar (TRM) as an overlay has become an important method for repairing and strengthening old masonry structures. However, the quantitative analysis and design of TRM-strengthened reinforced concrete (RC) beams are still limited. To address this gap, a nonlinear finite element (FE) model is proposed in this study to simulate the flexural behavior of TRM-strengthened RC beams. The developed model is validated using experimental results and subsequently utilized for the design of TRM-strengthened RC beams. Various TRM design parameters, including the number of textile layers, textile longitudinal length, and textile mesh size, are parametrically investigated. The modelling results reveal that increasing the number of textile layers and longitudinal length while decreasing the textile mesh size can enhance the bending strength of TRM-strengthened RC beams. Furthermore, an analytical model is proposed to predict the flexural strength of TRM-strengthened RC beams, facilitating rapid strength estimation of TRM-strengthened RC beams. The predicted results demonstrate good agreement with the numerical simulation results. The established FE models can predict the bending performance of TRM-strengthened RC beams under different reinforcement conditions, and the simulation outcomes can provide valuable guidance for their design.

1. Introduction

With the rapid economic development in China, numerous masonry structures are facing deterioration due to factors such as ageing of materials, environmental degradation, and lack of maintenance. To ensure their safety and extend their service life, it is necessary to repair and strengthen these structures through reliable and proper approaches [1]. Over the past decade, extensive research has been conducted on enhancing the flexural strength of structures using composites like fiber-reinforced polymer (FRP) [2–4], engineered cementitious composite [5,6], and textile reinforced mortar (TRM) [7,8], which cause minimal invasion. Among these, TRM, as an inorganic cementitious reinforcement material, has gained significant attention due to its effective, cost-efficient properties and good compatibility with the old concrete structure [9–12]. Additionally, incorporating various waste textile materials, such as discarded carpets and clothing, into TRM enhances its environmental friendliness [13–16].

TRM consists of textiles embedded in an inorganic matrix to form a mesh structure. The matrices used in TRM are mainly high-performance cement mortar and polymer-modified cement mortar [17–20], while the embedded high-strength textiles are usually made from carbon, glass, basalt, and aramid fiber [21–24]. Unlike FRP, which is installed using epoxy adhesive [25–27], TRM is directly adhered to the soffit of beams to integrate with concrete, serving the purpose of reinforcement or repair. Additionally, to prevent debonding between the TRM and the concrete surface, techniques such as replacing the matrix material, roughening the surface, or using mechanical anchorage have been employed [28–31].

Numerous experimental studies have investigated the strengthening of reinforced concrete (RC) beams, slabs and columns using TRM for

---

* Corresponding authors.
E-mail addresses: yuanzhidan9@163.com (Z. Yuan), zhi-fei.tan@connect.polyu.hk (Z. Tan).

https://doi.org/10.1016/j.matdes.2024.113227
Received 8 June 2023; Received in revised form 21 June 2024; Accepted 1 August 2024

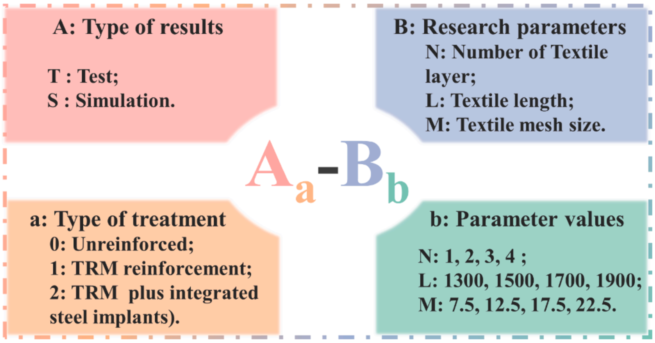

Fig. 1. Rule for naming the different beams in this study.

Table 1
Material properties used in the finite element modeling of TRM-strengthened beams.

Carbon fiber	
Material model	MAT_PIECEWISE_LINEAR_PLASTICITY
Fiber bundle bulk density (kg/m^3)	1780
Fiber bundle density (tex)	801
Tensile strength (MPa)	4660
Modulus of elasticity (GPa)	231
Alkali-free glass fiber	
Material model	MAT_PIECEWISE_LINEAR_PLASTICITY
Fiber bundle bulk density (kg/m^3)	2580
Fiber bundle density (tex)	1500
Tensile strength (MPa)	3200
Modulus of elasticity (GPa)	65
Note: tex indicates the mass (g) of 1000 m long fiber bundles. The tensile strength, elastic modulus, and elongation are the performance values of fiber monofilaments.	
Concrete	
Material model	MAT_CSCM_CONCRETE
Density (kg/m^3)	2330
Uni-axial compressive strength (MPa)	26.9
Mortar	
Material model	MAT_CSCM_CONCRETE
Density (kg/m^3)	1950
Uni-axial compressive strength (MPa)	53.3
Reinforcement in the tensile zone	
Material model	MAT_PIECEWISE_LINEAR_PLASTICITY
Diameter (mm)	12
Yield stress (MPa)	339.5
Ultimate tensile strength (MPa)	514.6
Modulus of elasticity (GPa)	200
Stirrups and reinforcement in the compression zone	
Material model	MAT_PIECEWISE_LINEAR_PLASTICITY
Diameter (mm)	6
Yield stress (MPa)	409.6
Ultimate tensile strength (MPa)	619.9
Modulus of elasticity (GPa)	210

various applications, including flexural reinforcement [32–34], shear reinforcement [35–38], seismic reinforcement [39–41], and column restraint [42–44]. Research on the flexural strengthening of RC beams has shown that TRM significantly improves flexural strength, reduces deflection, and limits crack width [45,46]. Moreover, TRM reinforced beams exhibit better ductility compared to those reinforced with FRP [47]. Studies indicate that the failure mode of TRM-strengthened RC beams tends to be slippage failure when reinforced with 1 or 2 layers of fibers; however, with 3 layers, failure is primarily due to delamination between the fiber and the cementitious matrix [48]. Furthermore, fiber debonding is a critical consideration in TRM reinforcement of RC beams. D' Ambrisi et al. [49] found that the failure of TRM-strengthened systems occurred at the textile/matrix interface rather than due to concrete debonding. Raoof et al. [50] reported that the reinforcing effect of TRM was sensitive to the number of layers, with the effectiveness factor—the ratio of the flexural capacity increase achieved by TRM to that achieved by equivalent FRP—increasing from 0.47 to 0.80 as the number of TRM layers increased from 1 to 3. Schladitz et al. [51] used TRM to reinforce a floor slab, observing a significant increase in bearing capacity and a reduction in deflection. These studies highlight the substantial impact of textile parameters on the flexural performance of TRM-strengthened RC beams. However, a systematic approach to evaluating these parameters' effects on TRM-strengthened RC beams remains lacking.

Determining design parameters through experimental tests is time-consuming and resource-intensive. Numerical modelling has emerged as a promising tool for the design of TRM-strengthened RC beams. Elsanadedy et al. [47] utilized an explicit nonlinear FE model to simulate the flexural performance of RC beams reinforced with different TRM schemes. Their findings indicated that U-shaped anchorage at the end of the TRM layer could effectively prevent or delay end debonding. Portal et al. [52] conducted detailed modeling of carbon textile-reinforced slabs, evaluating the influence of material characteristics and interface bonding on flexural performance. Colombo et al. [53] established a FE model of reinforced beams, considering material nonlinearity and geometric nonlinearity, to investigate the bending behavior of sandwich beams. The results demonstrated that the response of the overall sandwich layer of the reinforced beam is predominantly controlled by the nonlinear behavior of foamed polyethylene and the bending behavior of textile-reinforced concrete, rather than by the position of the textile in the outer layer. Parvin and Alhusban [54] employed nonlinear FE analysis to investigate the effects of parameters such as beam depth, load distributions, and orientations and stacking sequences of the textile's mesh layers on the shear performance of TRM-strengthened RC beams. Despite these advancements, a comprehensive investigation into the design of TRM-strengthened RC beams based on FE methods remains lacking.

Therefore, the aim of this study is to propose numerical modelling methods for the computational design of TRM-strengthened RC beams. To achieve this purpose, refined three-dimensional FE models of RC beams strengthened with different TRM designs were developed. An elastoplastic damage constitutive model was applied to capture the nonlinearity of concrete and textile mortar. The FE models simulated the failure mechanisms and characteristics of TRM-strengthened RC beams, which were subsequently validated against experimental results. Based on the validation, the FE model was further employed to investigate the effects of different TRM design parameters, including the number of textile layers, textile longitudinal length, and textile mesh size on the flexural performance of TRM-strengthened RC beams. Moreover, an analytical model was derived and verified using the modelling results to enable rapid analysis of the load capacity of TRM-strengthened RC beams. For clarity, the beams discussed hereafter are labeled as shown in Fig. 1. For instance, T_1-N_3 represents an experimental RC beam reinforced with a three-textile-layer TRM.

2. Materials and experimental program

This section details the fabrication of unreinforced RC beams and two types of reinforced RC beams (TRM and TRM plus integrated steel implants) with 3 textile layers for four-point bending tests. These beams are labeled as T_0, T_1-N_3 and T_2-N_3.

2.1. Preparation of textile mesh

The textile mesh used for TRM was composed of carbon fiber bundle and alkali-free glass fiber bundle. Each fiber bundle was made up of several single fibers, and their physical and mechanical properties are presented in Table 1. Fig. 2a shows the used textile mesh with a mesh size of 12.5 mm × 12.5 mm. Carbon fiber bundles were aligned longitudinally, while alkali-free glass fiber bundles were aligned transversely, and the junctions were stitched with yarn. Epoxy resin was then applied to the textile mesh (Fig. 2b) to enhance the integrity of the fiber bundles and reduce uneven stress transfer between the matrix and fibers [55,56]. The tensile strength of the epoxy resin-treated fiber bundle was tested

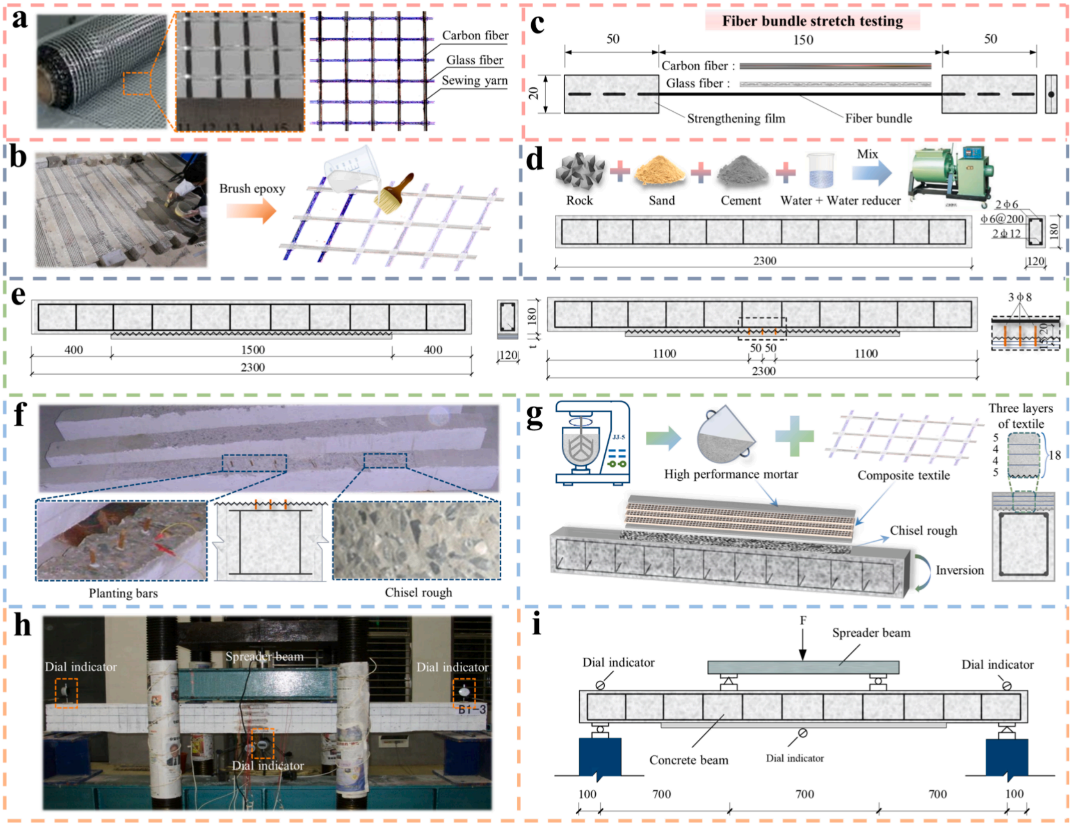

Fig. 2. Testing and loading process: (a) Textiles; (b) Textile treated with epoxy resin; (c) Tensile test of a single fiber bundle; (d) Material and dimensions of RC beam; (e) Details and scope of textile layering; (f) Surface roughening and steels implanting of RC beams; (g) Layering process of textile; (h) On-site testing process; and (i) Schematic of loading device. (All units are mm).

[57], as shown in Fig. 2c. It found that the ultimate tensile strength of a single carbon fiber bundle and alkali free glass fiber bundle can reach 1428 N and 552 N, respectively.

2.2. Preparation of RC beam

Fig. 2d illustrates the process for the RC beam preparation. C25 concrete, with a compressive strength of 26.9 MPa after 28 days of curing, was used for the beams. HRB335 steel was employed for reinforcement in the tensile zone, and HRB400 steel was used for stirrups and reinforcement in the compression zone. Their mechanical properties are detailed in Table 1. The beams measured 2300 mm in length and had a cross-section of 120 mm × 180 mm (width × depth).

2.3. Preparation of TRM reinforced RC beam

Previous tests showed that TRM-strengthened RC beams with multiple textile layers were well-bonded at both ends, but horizontal debonding cracks occurred at the bond interface in areas with high bending moments due to insufficient shear resistance. To prevent such phenomena, the reinforcement section at the bottom of the RC beam was roughened, and three steel bars were implanted in the middle of the span. The details are shown in Fig. 2e. The surface roughening was carried out by using a hammer and chisel to strike the bottom surface of the reinforced section to form random concave and convex shapes, as shown in Fig. 2f. The sand-filling method was used to quantify the surface roughness of the RC beams by measuring the average sand-filling depth using Eq. (1) [58]. The value of H_s in this study was taken as 3.3 (±0.3) to ensure that the surface of the RC beams was not significantly damaged.

$$H_s = \frac{V_s}{A_s} \tag{1}$$

where H_s is the average sand-filling depth (mm), V_s is the volume of sand (mm^3), and A_s is the area of the treated concrete substrate (mm^2).

After the surface roughing and implanting of steels, the reinforcement section was cleaned with steel brush and blower and then wetted with water. The TRM was then applied to the bottom of the RC beam. The TRM matrix material was M50 high-performance mortar, with a measured compressive strength of 53.3 MPa for a 28-day cube specimen. As shown in Fig. 2g, the production of TRM-strengthened RC beam is as follows: 1) a 5 mm layer of high-performance mortar was poured to the bottom surface of the reinforcement section; 2) the textile was laid on the mortar and a spatula was used to press the textile slightly into the mortar; 3) a 4 mm layer of mortar was poured, and step 2 was repeated according to the target number of layers for different samples; 4) after the last layer of textile was laid, a final 5 mm layer of mortar was applied.; and 5) the beams were covered with plastic sheeting for curing until the test age.

2.4. Flexural strength testing

Four-point flexural testing was performed to evaluate the flexural strength of TRM-strengthened RC beams. Fig. 2h shows the test in process, and Fig. 2i illustrates the test setup. In the test, a preload of 3 kN was first applied to eliminate any gaps between the sample and the loading device. Subsequently, a step-loading pattern with an interval of 3 kN was adopted. Each loading level was maintained for 3–5 mins to record test results and observe crack propagation. The load versus mid-span displacement response curves of the TRM-strengthened RC beams were obtained from this testing procedure.

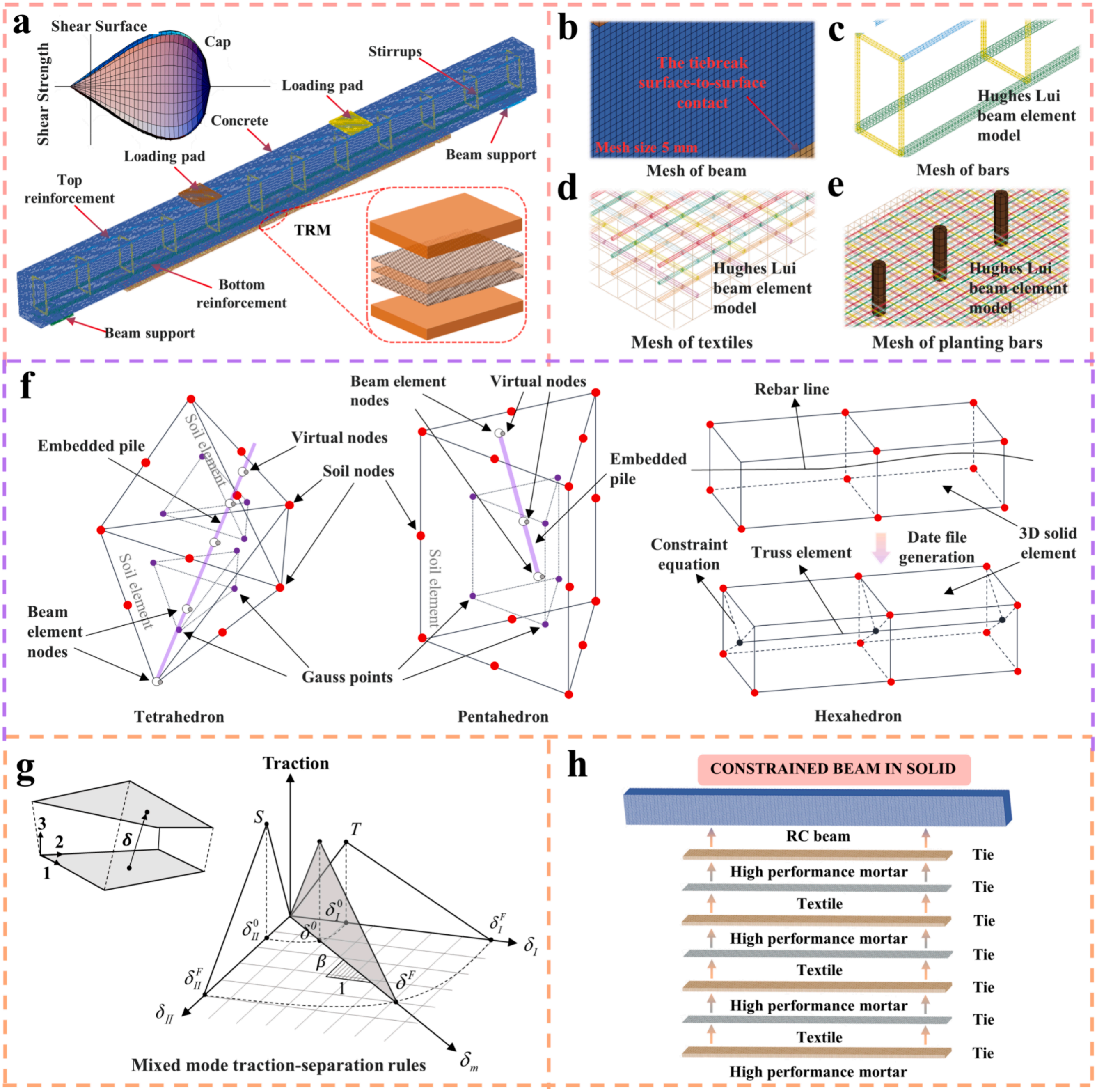

Fig. 3. Details of FE model establishment: (a) TRM-strengthened RC beam model and Cap model; (b) RC beam matrix and TRM mesh division; (c) Division of steel reinforcement; (d) Mesh division of textiles; (e) Mesh division of integrated steel implants; (f) The implanting methods of steel in different elements; (g) Mixed mode traction-separation rules; (h) Schematic of three-textile-layer TRM-strengthened RC beam model; (i-k): Three FE model diagrams: S_0, S_1-N_3, and S_2-N_3.

3. Finite element model development

This section focuses on establishing the FE model for the TRM-strengthened RC beam. The material models used, and the simulation settings are discussed in detail.

3.1. Material modelling

The material parameters used to build the finite element model are summarized in Table 1. To simulate the bending failure of RC beams during testing, the MAT_CSCM_CONCRETE material model (No. 159) in the LS-DYNA software was employed for the high-performance mortar in the RC beam. Fig. 3a illustrates the yield surface of the Cap model, where the initial damage surface aligns with the yield surface, and the viscoplastic model incorporates rate effects. The following equations define the invariants using the deviatoric stress tensor S_{ij} and the hydrostatic pressure P:

$$J_1 = 3P \tag{2}$$

$$J_2' = \frac{1}{2}S_{ij}S_{ij} \tag{3}$$

$$J_3' = \frac{1}{2}S_{ij}S_{ij}S_{ij} \tag{4}$$

where J_1 = the first invariant of the stress tensor; J_2' = the second

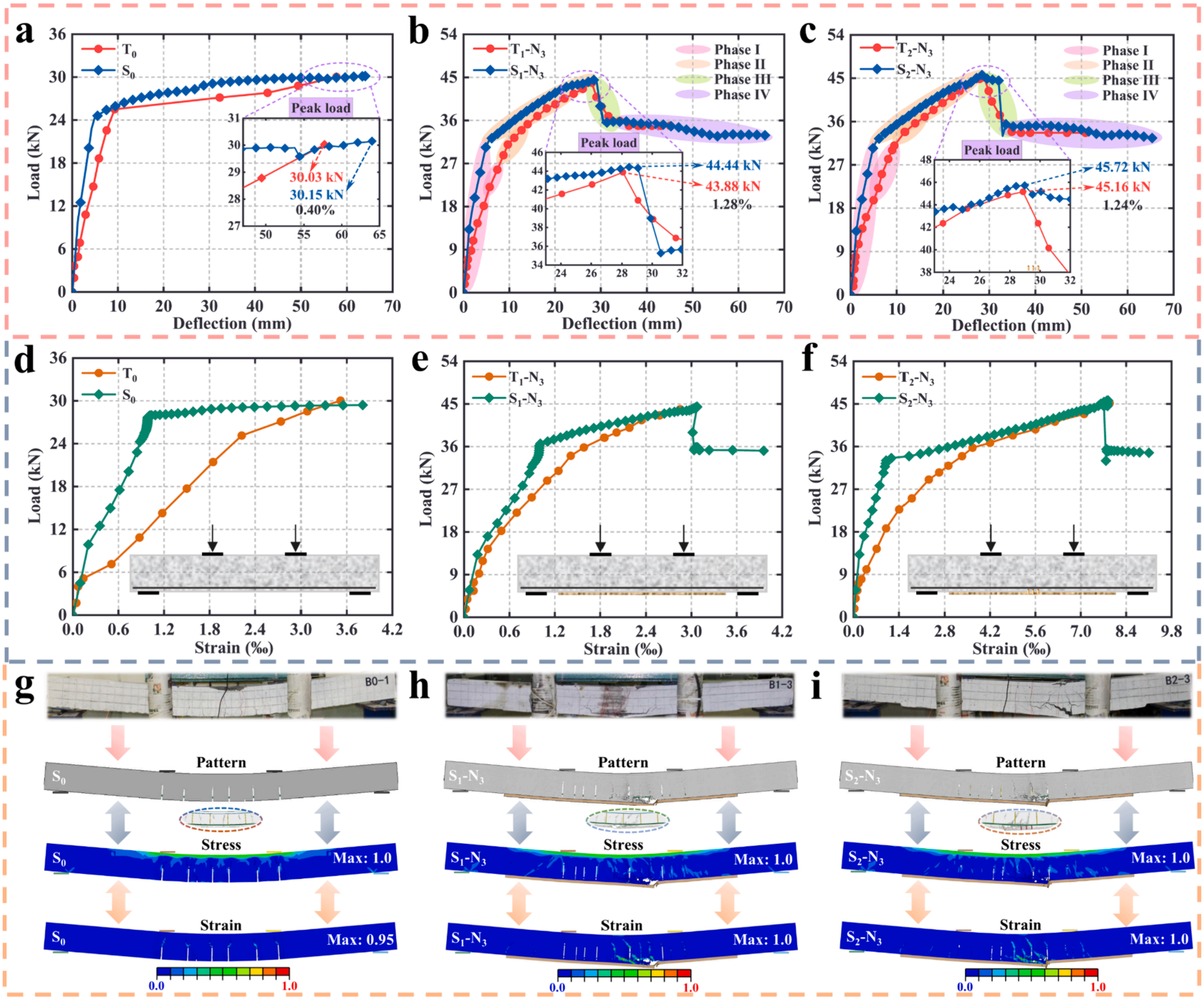

Fig. 4. Comparison between experimental test and simulation results: (a-c) Load-deflection curve; (d-f) Mid-span strain curve of tensile steel; (g-i) Comparison of failure mode between experimental test and simulation models: (g) S_0; (h) S_1-N_3; (i) S_2-N_3.

Table 2
Effect of the number of textile layers.

Specimen name	Number of textile layers	Thickness of TRM (mm)	Length of implanted steels in TRM (mm)	P_u (kN)	% P_u increase ratio to S_0	Δ_u (mm)
S_0	–	–	–	30.15	–	64.01
S_1-N_1	1	10	7	33.71	11.81	20.20
S_1-N_2	2	15	12	39.10	29.68	25.79
S_1-N_3	3	18	15	44.44	47.70	28.47
S_1-N_4	4	20	17	49.77	65.07	29.37
S_2-N_1	1	10	7	32.17	6.70	32.54
S_2-N_2	2	15	12	36.26	20.27	33.14
S_2-N_3	3	18	15	45.72	51.64	28.98
S_2-N_4	4	20	17	48.80	61.86	28.88

Note: The textile length and mesh size for all reinforced beams are 1500 mm and 12.5 mm × 12.5 mm, respectively. The reinforcement ratio of the RC beam is 1.047 %.

invariant of the deviatoric stress tensor; and $J_3' =$ the third invariant of the deviatoric stress tensor. The yield function is constructed based on stress invariants, and the cap hardening parameter K is introduced into the yield surface to account for failure behavior due to triaxial compression, as shown in Equation (5):

$$f(J_1,\ J_2',\ J_3',\ K) = J_2' - R^2 F_f^2 F_c \tag{5}$$

where F_f is the shear failure surface; F_c is the hardening cap; R is the reduction factor of three Rubin invariants. The cap hardening parameter K is the value of the pressure invariant at the intersection of the cap and the shear surface. The strength of concrete under tensile and low confining pressures is simulated by shear planes. The shear surface F_f is defined along the compression meridian, as shown in Eq. (6).

$$F_f\ (J_1) = \alpha \text{ - } \lambda \exp^{-\beta J_1} + \theta J_1 \tag{6}$$

The values of α, β, λ and θ of models were determined through fitting strength values of plain concrete cylinders obtained with test results. The concrete strength was determined by considering the combination of caps and shear surfaces at different confining pressures. The cap in the strength criterion is used to model the plastic volume change associated

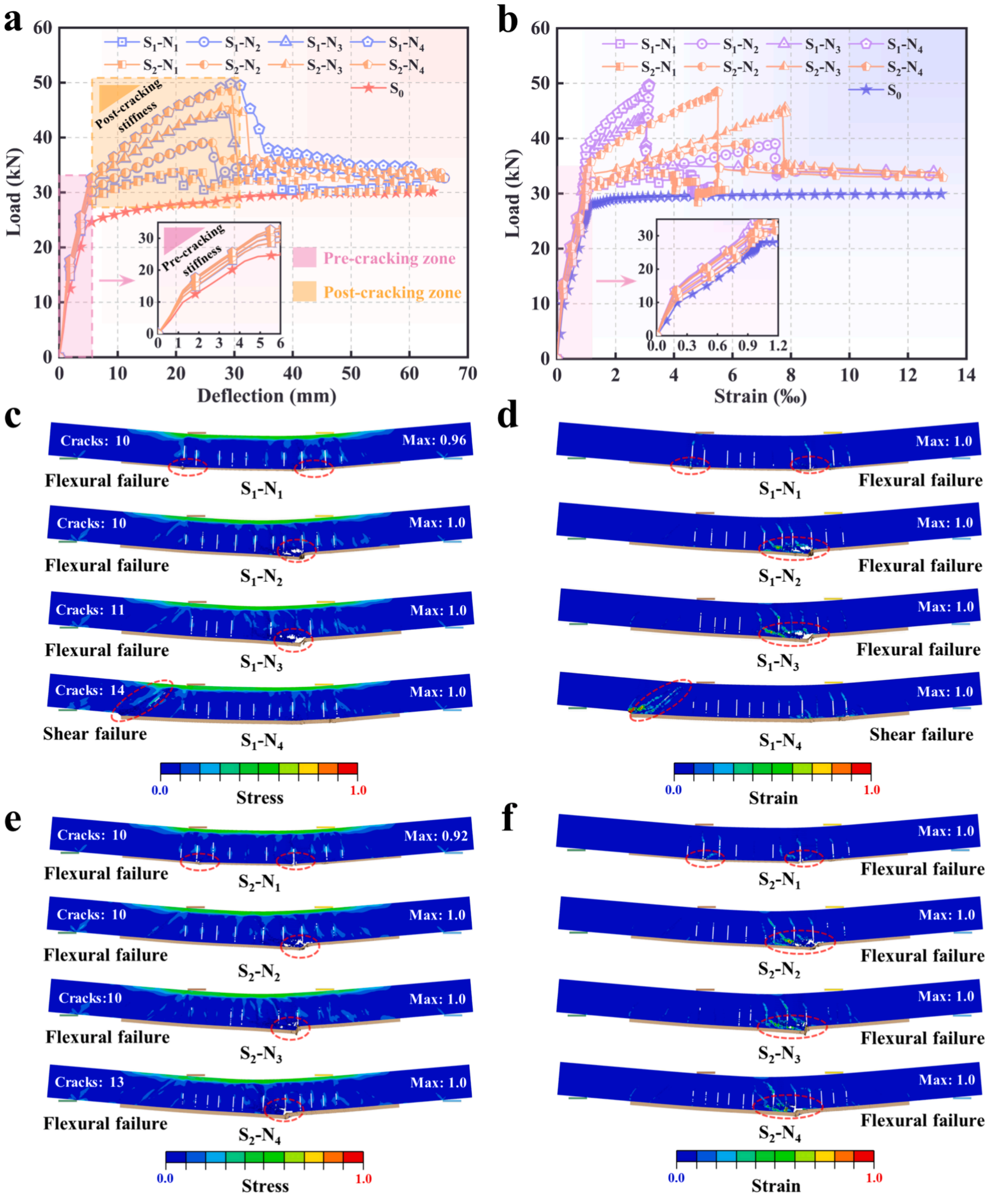

Fig. 5. Influence of the number of textile layers on the flexural performance of reinforced RC beams: (a) Load-deflection curve; (b) Mid-span strain curve of tensile steel; (b) Mid-span strain curve of tensile steel; (c) Stress cloud maps of RC beams reinforced by TRM; (d) Strain cloud maps of RC beams reinforced by TRM; (e) Stress cloud maps of RC beams reinforced by TRM plus integrated steel implants; (f) Strain cloud maps of RC beams reinforced by TRM plus integrated steel implants.

with pore collapse, even though the pores were not explicitly simulated. The initial position of the cap determines the onset of plastic deformation under isotropic compression. The cap reflects the reinforcement characteristics under triaxial compression, which involve volume and strain reinforcement caused by the water purification pressure. The plastic surface of the cap transforms into a failure surface when it cannot move [59,60].

The RC beam model was meshed using cube elements with a size of 5 mm, as depicted in Fig. 3b. The 2-node Hughes-Lui beam elements [61] can simulate rectangular and circular cross sections using a set of integration points in the middle span of the beam element, which are suitable for simulating materials with arbitrary elastic–plastic stress–strain

Table 3
Effect of the length of longitudinal textile.

Specimen name	Longitudinal length of textile (mm)	P_u (kN)	% P_u increase with respect to S_0	Δ_u (mm)
S_0	–	30.15	–	64.01
S_1-L_{1300}	1300	39.62	31.41	29.77
S_1-L_{1500}	1500	44.44	47.40	28.47
S_1-L_{1700}	1700	47.73	58.31	32.90
S_1-L_{1900}	1900	49.31	63.55	35.45
S_2-L_{1300}	1300	39.52	31.08	28.60
S_2-L_{1500}	1500	45.72	51.64	28.98
S_2-L_{1700}	1700	48.00	59.20	32.29
S_2-L_{1900}	1900	47.64	58.01	31.59

Note: The thickness of TRM and the length of implanted steels in TRM for all reinforced beams are 18 mm and 15 mm, respectively. The textile layer and mesh size for all reinforced beams are 3 and 12.5 mm × 12.5 mm, respectively, and the reinforcement ratio of the RC beam is 1.047 %.

curves and strain rate dependence. Therefore, the longitudinal steel bars, stirrups, fiber bundle and implanted steels were represented in the model using 2-node Hughes-Lui beam elements with 2 × 2 Gauss quadrature integration at the cross-section. The fiber bundle and implanted steels in the composite textile layer were defined using the bilinear elastic–plastic constitutive method, as depicted in Fig. 3(c-e). In the TRM-strengthened RC beam, the composite textile layers were arranged in two orthogonal directions and embedded within the isotropic mortar material. The beam element diameters for the carbon fiber bundle and glass fiber bundle were determined by converting them into equivalent circular sections based on the linear density of materials provided in Table 1, resulting in diameters of 0.757 mm and 0.860 mm, respectively.

3.2. Contact modelling

To establish the connection between the steel elements and the surrounding concrete elements, the CONSTRAINED BEAM-IN-SOLID function in LS-DYNA was utilized. This function ensures the conservation of kinetic energy in the FE calculation by binding the motion of the beam structure to that of the Lagrangian solid or thick shell, serving as the main surface. The motions considered include acceleration and velocity. The contact between the steel bar and concrete elements is explained using the piling concept introduced by Tschuchnigg and Schweiger [62].

$$R_{eq} = \max\left\{\sqrt{\frac{A}{\pi}}, \sqrt{\frac{I_2 + I_3}{A}}\right\} \tag{7}$$

where, R_{eq} is the equivalent diameter of the embedded steel bar; A is the cross-sectional area of the embedded steel; and I_2 and I_3 are the moments of inertia in two directions. The embedded interface elements are used to account for relative displacements ($\mathbf{u}_{rel}$) between the embedded pile and the surrounding soil.

$$\mathbf{t}^{skin} = \mathbf{T}^{skin}\cdot\mathbf{u}_{rel} \tag{8}$$

$$\mathbf{t}^{skin} = \begin{bmatrix} t_s \\ t_n \\ t_t \end{bmatrix} \tag{9}$$

$$\mathbf{T}^{skin} = \begin{bmatrix} K_s & 0 & 0 \\ 0 & K_n & 0 \\ 0 & 0 & K_t \end{bmatrix} \tag{10}$$

$$\mathbf{u}_{rel} = \begin{bmatrix} u_s^p - u_s^s \\ u_n^p - u_n^s \\ u_t^p - u_t^s \end{bmatrix} \tag{11}$$

where $\mathbf{t}^{skin}$ is the skin traction along the embedded pile and the $\mathbf{T}^{skin}$ matrix contains the stiffnesses of the embedded interface element; t_s is the axial shear stress; t_n and t_t are the normal stresses of embedded steel; K_s is the stiffness of the axial interface; K_n and K_t are the stiffnesses of normal interfaces; u_s and u_p are the displacements of virtual nodes and embedded elements, respectively.

$$t_{s,max} = \left(\sigma'^{\,avg}_{n}\cdot\tan\varphi'_i + c'_i\right)\cdot 2\cdot\pi\cdot R_{eq} \tag{12}$$

$$\sigma'^{\,avg}_{n} = \frac{\sigma'_t + \sigma'_n}{2} \tag{13}$$

where $t_{s,max}$ is the maximum shear stress of the pile; φ'_i and c'_i are the strength parameters of the pile-soil interface; $\sigma_n^{'avg}$ is the normal stress along the pile-soil interface; σ'_t and σ'_n are the effective stresses perpendicular to the steel.

$$K_s = \alpha_s\cdot G_{el}^{av}\cdot\Gamma_s + \Delta_s \tag{14}$$

$$K_n = K_t = \alpha_s\cdot G_{el}^{av}\cdot\frac{2(1-\nu_i)}{1-2\cdot\nu_i}\Gamma_n + \Delta_n \tag{15}$$

$$K_{base} = \alpha_{base}\cdot G_{el}^{av}\cdot R_{eq}\cdot\Gamma_{base} \tag{16}$$

where Γ_s is the multiplier of the shear modulus of the axial interface stiffness; Γ_n is stiffness of the normal and tangential interface; Γ_{base} is the stiffness of base interface; Δ_s and Δ_n are the input values of K_s and K_s/K_t, respectively; α_s and α_{base} are dimensionless interface stiffness factors of axial and substrate nested interface stiffness. the G_{el}^{av} is the average shear stiffness of the allocated soil element, is used to define the embedded interface stiffnesses. Fig. 3f illustrates the methods used for integrated steel implants in different concrete elements. Similar approaches were employed for the bonding between high-performance mortar and composite textiles, as well as the bonding between integrated steel implants and mortar in TRM.

The bonding between concrete and high-performance mortars was defined by the separation CONTACT model, whose keyword in LS-DYNA is CONTACT-AUTOMATIC-ONE-WAY-SURFACE-TO-SURFACE-TIEBREAK. This contact mode adopts Dycoss discrete crack model of power law and B-K damage model, which shares the same contact algorithm with ordinary contact mode under compressive load. This contact algorithm also considers both normal and shear forces at the interface. When subjected to tensile and shear loads, the failure and separation can be determined by the interfacial tensile strength criteria. The failure criterion is defined by the bilinear traction-separation criterion combined with quadratic mixing and damage variable. The mixed traction-separation rule is shown in Fig. 3g. The material model was used together with the cohesive element formulation to simulate the interface behavior. According to the failure criterion, the limit displacement at normal and tangential directions of the interface is the displacement when the material fails completely and the traction force drops to 0. The relationship between energy release rate, peak traction force and, limit displacement during interfacial fracture can be defined as:

$$G_{Ic} = T \times \frac{U_{ND}}{2} \tag{17}$$

$$G_{IIc} = S \times \frac{U_{TD}}{2} \tag{18}$$

where G_{Ic} and G_{IIc} are the energy release rates of type I and type II fracture, respectively; T is the peak normal traction force; S is the peak tangential traction force; U_{ND} is the normal limit displacement; and U_{TD}

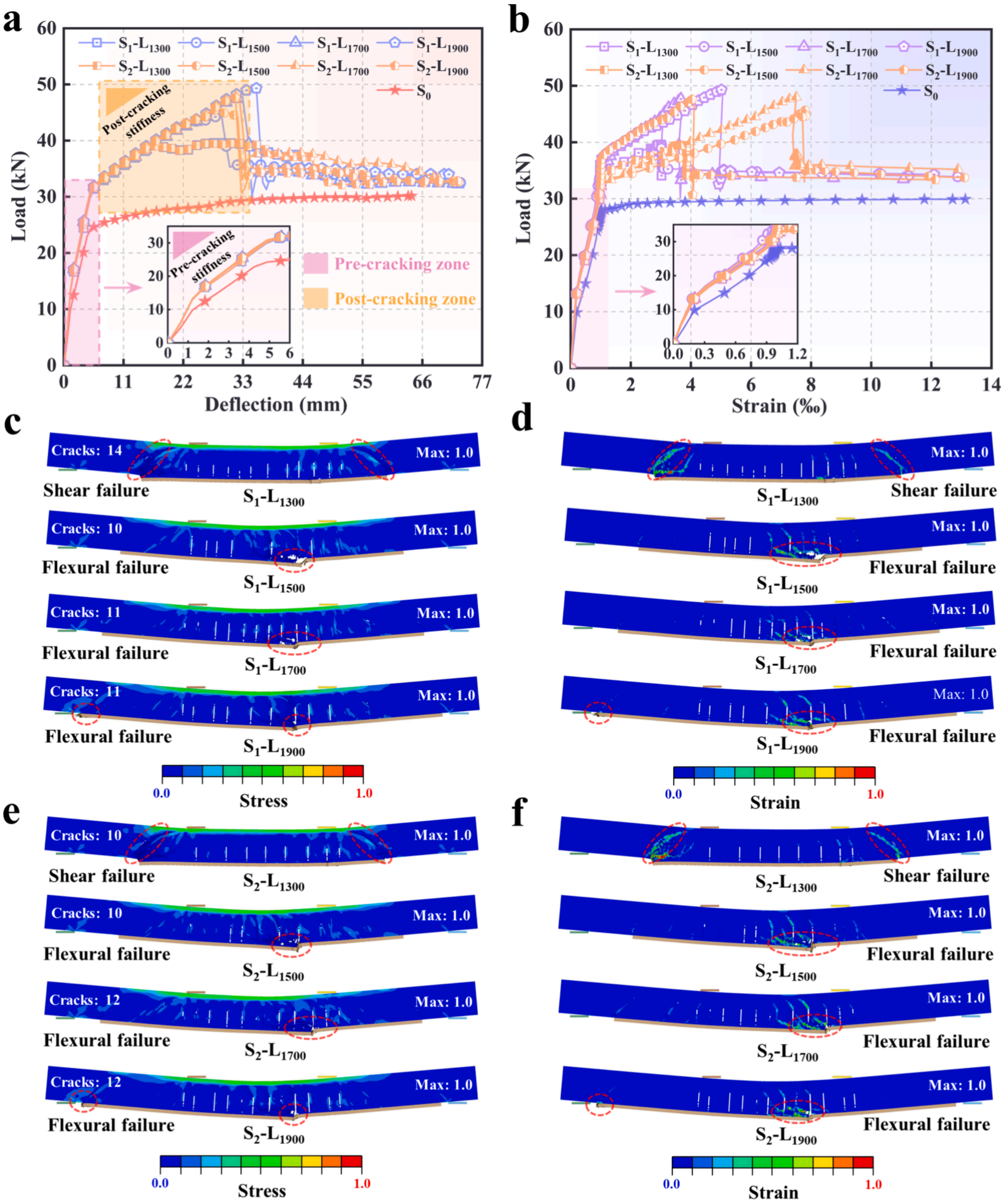

Fig. 6. Influence of the longitudinal length of textile on the flexural performance of TRM-strengthened RC beams: (a) Load-deflection curve; (b) Mid-span strain curve of tensile steel; (c) Stress cloud maps of RC beams reinforced by TRM; (d) Strain cloud maps of RC beams reinforced by TRM; (e) Stress cloud maps of RC beams reinforced by TRM plus integrated steel implants; (f) Strain cloud maps of RC beams reinforced by TRM plus integrated steel implants.

is the tangential limit displacement.

In the cohesive material model, the relative displacement of the total mixing mode δ_m is defined by the following equation.

$$\delta_m = \sqrt{\delta_{\mathrm{I}}^2 + \delta_{\mathrm{II}}^2} \tag{19}$$

$$\delta_{\mathrm{II}} = \sqrt{\delta_1^2 + \delta_2^2} \tag{20}$$

where $\delta_I = \delta_3$, which is the separation in the normal direction (mode I); and δ_{II} is the separation in the tangent direction. The initial displacement of the mixed mode damage is given by Eq. (21).

Table 4
Effect of the mesh size.

Specimen name	Mesh size (mm)	P_u (kN)	% P_u increase with respect to S_0	Δ_u (mm)
S_0	–	30.15	–	64.01
S_1-$M_{7.5}$	7.5 × 7.5	54.81	81.79	28.72
S_1-$M_{12.5}$	12.5 × 12.5	44.44	47.40	28.47
S_1-$M_{17.5}$	17.5 × 17. 5	44.35	48.09	38.29
S_1-$M_{22.5}$	22.5 × 22.5	44.21	46.63	39.51
S_2-$M_{7.5}$	7.5 × 7.5	54.94	82.22	28.63
S_2-$M_{12.5}$	12.5 × 12.5	45.72	51.64	28.98
S_2-$M_{17.5}$	17.5 × 17. 5	44.36	47.13	36.96
S_2-$M_{22.5}$	22.5 × 22.5	44.28	46.87	39.90

Note: The thickness of TRM and length of implanted steels in TRM for all reinforced beams are 18 mm and 15 mm, respectively. The textile layer length for all reinforced beams is 1500 mm, and the reinforcement ratio of the RC beam is 1.047 %.

$$\delta^0 = \delta_{\mathrm{I}}^0 \delta_{\mathrm{II}}^0 \sqrt{\frac{1 + \beta^2}{\left(\delta_{\mathrm{II}}^0\right)^2 + \left(\beta \delta_{\mathrm{I}}^0\right)^2}} \tag{21}$$

$$\delta_{\mathrm{I}}^0 = T/EN \tag{22}$$

$$\delta_{\mathrm{II}}^0 = F/TN \tag{23}$$

where δ^0 is the initial displacement when the softening occurs; δ_{I}^0 and δ_{II}^0 are the initial and final separation of the damage model; *EN* is the stiffness perpendicular to the surface of cohesive units; TN is the stiffness of the cohesive unit's surface; $\beta = \delta_{\mathrm{II}}/\delta_{\mathrm{I}}$ represents the mixed mode, as shown in Fig. 3g. The limit mixing mode displacement δ^{F} (complete failure) can be given by the power law ($XMU > 0$) or Benzeggagh-Kenane law ($XMU < 0$), as shown in Eqs (24–25), respectively [63].

$$\delta^{\mathrm{F}} = \frac{2\left(1 + \beta^2\right)}{\delta^0}\left[\left(\frac{EN}{G_{\mathrm{Ic}}}\right)^{XMU} + \left(\frac{ET \times \beta^2}{G_{\mathrm{IIc}}}\right)^{XMU}\right]^{-\frac{1}{XMU}} \tag{24}$$

$$\delta^{\mathrm{F}} = \frac{2}{\delta^0\left(\frac{1}{1+\beta^2} EN^{\gamma} + \frac{\beta^2}{1+\beta^2} ET^{\gamma}\right)^{1/\gamma}}\left[G_{\mathrm{Ic}} + \left(G_{\mathrm{IIc}} - G_{\mathrm{Ic}}\right)\left(\frac{\beta^2 \times ET}{EN + \beta^2 \times ET}\right)^{|XMU|}\right] \tag{25}$$

where *XMU* is the index of the mixed mode criterion; γ is an index in Benzeggagh-Kenane law, which can be taken as 1.0 or 2.0.

It is worth noting that the presence of integrated steel implants significantly enhances the strength of the interface layer between the substrate concrete and TRM. Consequently, for the simulation, their contact was assumed to be fully bonded.

3.3. Damage definition

The erosion occurring between RC and high-performance mortar elements was simulated using the erosion option in LS-DYNA [47]. This option incorporates a method that accounts for material model failure and concrete spalling. When the erosion function is activated, the damaged solid element can be physically separated from the rest of the grid. Thus, whenever an element reaches its critical value, it is removed from the calculation. However, this damage mode results in discontinuous deformation, leading to singularity in the grid Jacobian matrix. A viscosity coefficient of 0.0001–0.001 is set to ensure convergence of the calculation. In concrete and mortar failure simulation, an element is deleted when the maximum principal strain reaches 0.05, and the damage value reaches 1 [60].

3.4. Loading method

The loading method used in the experimental tests was a forward monotonic grading loading mode. However, it is difficult to simulate the softening process, swaying behaviour and structural collapse of the beam structure during the final stage in the FE simulations using this loading mode. An accelerated loading method based on the explicit dynamics algorithm was employed to reproduce the above mentioned damage process of the beam structure. This method applies the load to the top of the beam through forced displacement. However, this loading method may introduce inertial effects. Fortunately, this effect can be minimized by appropriately selecting the physical time. Trial simulations have shown that adopting a physical time of 1.0 s resulted in kinetic energy induced by inertia effects being less than 5 % of the total energy.

3.5. Model development of the experiments

The configuration of the composite textile layer in TRM and the schematic of three-textile-layer TRM-strengthened RC beam model are illustrated in Fig. 3a and 3 h. Using the numerical methods described above, three groups of FEM beam models were established corresponding to the test beams (S_0, S_1-N_3, and S_2-N_3), as depicted in Fig. 3(i-k). Notably, the integrated steel implants used in the test beams was also considered in the FE models. Taking S_2-N_3 as an example, the total number of 3D elements for concrete and high-performance mortar are 397,440 and 21,600, respectively. Additionally, there are 2,720 beam elements for longitudinal steel and 7,070 for stirrups, as well as 21 elements for each layer of textile and integrated steel implants. It is important to note that the element count mentioned above varies based on the textile parameters and the thickness of the high-performance mortar.

4. Finite element model validation

To validate the proposed modelling method, the corresponding FE beam models (S_0, S_1-N_3 and S_2-N_3) to the experimental ones (T_0, T_1-N_3 and T_2-N_3) were constructed and simulated.

Fig. 4(a-c) illustrates the load–deflection curves for the three cases. From Fig. 4a, it can be found that the predicted flexural failure curve for the RC beam without TRM agrees well with the experimental curve, demonstrating the effective prediction of bending failure for RC beams by this model. Fig. 4b and Fig. 4c present the flexural failure curves of the TRM-strengthened RC beams. Generally, the failure curve can be divided into four stages: (I) un-cracking stage, (II) cracking propagation until the peak loading stage, (III) sharp unloading stage, and (IV) steady stage [17,31,64–66]. From Fig. 4b and Fig. 4c, it is evident that both the experimental and simulated load–deflection curves for the TRM-strengthened RC beams exhibit these typical four stages. The agreement between the experimental and simulated curves indicates the high reliability and accuracy of the established FE models in predicting the bending failure of TRM-strengthened RC beams. Additionally, Fig. 4(d-f) depict the strain-load curves for both test and modelling of the steel. Although there is some variability in the simulated strain variation of the reinforcement in the initial stage compared to the experimental tests, the strain at the fracture of the steel remains nearly the same.

Furthermore, Fig. 4(g-i) shows failure samples from the experimental and simulation results. In Fig. 4g, the failure modes of the unreinforced beam in both experimental tests and simulation are in good agreement, where the concrete was crushed in the compression zone after the yield of the tensile steel. For the TRM-strengthened beams, as shown in Fig. 4h and Fig. 4i, the failure mode in the experimental test started with debonding and failure of the TRM, followed by failure of the beam matrix. The simulation demonstrates the rapid tensile yield of the steel once the textile in TRM fails. Compared to the beam without TRM, the cracks in reinforced beams at failure were smaller and denser, indicating

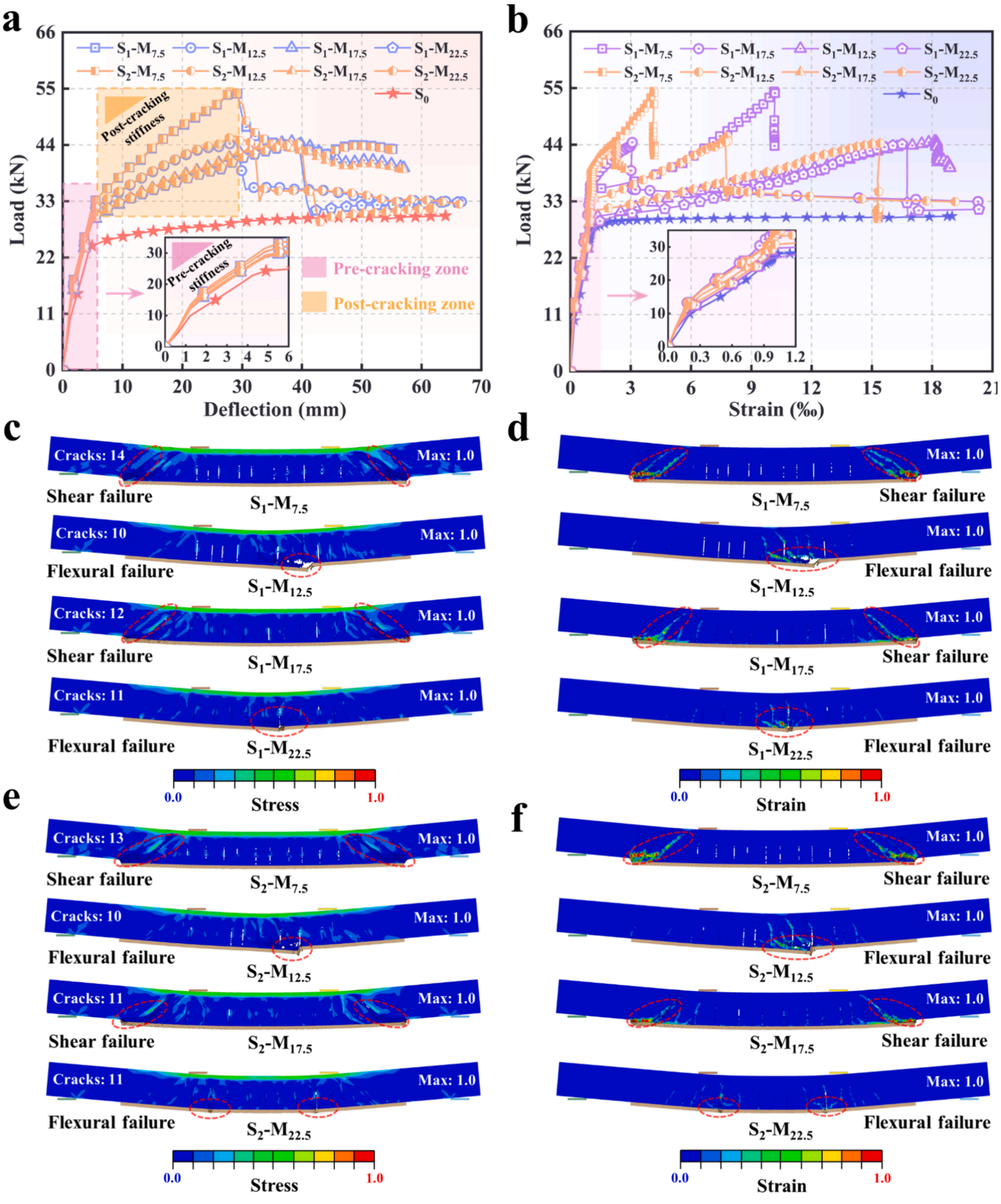

Fig. 7. Influences of the textile mesh size on the flexural performance of TRM-strengthened RC beams: (a) Load-deflection curve; (b) Mid-span strain curve of tensile steel; (c) Stress cloud maps of RC beams reinforced by TRM; (d) Strain cloud maps of RC beams reinforced by TRM; (e) Stress cloud maps of RC beams reinforced by TRM plus integrated steel implants; (f) Strain cloud maps of RC beams reinforced by TRM plus integrated steel implants.

that TRM reinforcement can reduce crack propagation in the beam [31,67]. Moreover, Fig. 4h and Fig. 4i reveal that the integrated steel implants have a slight effect on the stress distribution in reinforced RC beams during damage, with the range of cracks mainly localized around the positions where the steels were implanted.

The above results and analyses confirm that the FE model proposed in this paper has high consistency and accuracy in simulating the bending ultimate load and failure mode of beams. This model can be used as an effective tool to predict the bending failure response of TRM-strengthened RC beams. In section 5, the design-oriented parametric study of TRM-strengthened RC beams based on the developed FE models is performed.

5. Parametric study based on the developed FE model

To evaluate the influence of TRM on the flexural performance of

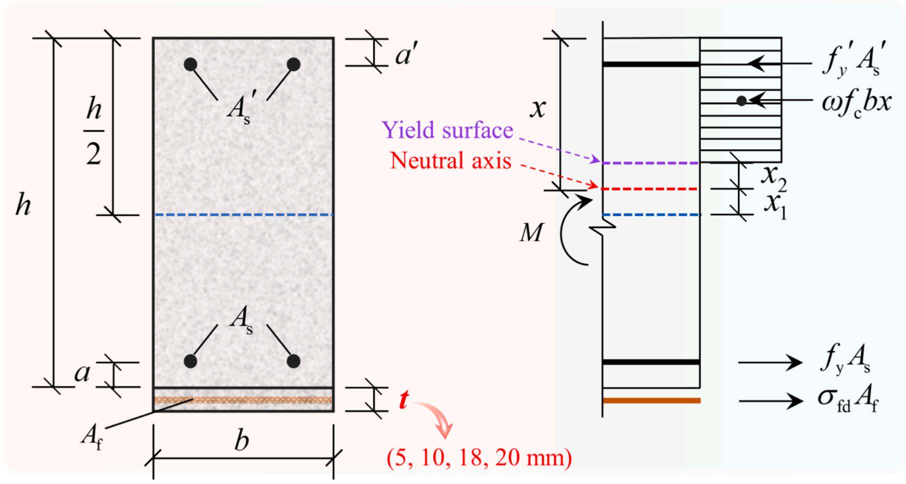

Fig. 8. TRM-strengthened RC beams cross-sectional force analysis and results prediction: (a) Beam section zoning and TRM-strengthened RC beam force equilibrium diagram.

Table 5
Comparison of flexural strength predictions from analytical model and FE model.

Specimen name	x (mm)	$M_{u,cal}$ (kN·m)	$M_{u,FE}$ (kN·m)	$M_{u,cal}$/ $M_{u,FE}$
S_1-N_1	149.18	11.07	11.80	0.94
S_1-N_2	140.50	12.86	13.69	0.94
S_1-N_3	127.73	14.50	15.55	0.93
S_1-N_4	119.47	16.47	17.42	0.95
S_1-L_{1300}	99.33	14.01	13.87	1.01
S_1-L_{1500}	127.73	14.50	15.55	0.93
S_1-L_{1700}	139.16	15.26	16.71	0.91
S_1-L_{1900}	148.34	15.77	17.26	0.91
S_1-$M_{7.5}$	101.70	18.33	19.18	0.96
S_1-$M_{12.5}$	127.73	14.50	15.55	0.93
S_1-$M_{17.5}$	145.98	13.70	15.52	0.88
S_1-$M_{22.5}$	153.75	13.45	15.47	0.86

reinforced RC beams, a parametric study is conducted using validated FE models. Three design parameters of TRM, namely the number of textile layers, the longitudinal length of the textile, and mesh size, are investigated. Modelling results are presented and analyzed to assess the design of TRM-strengthened RC beams.

5.1. *Textile layer*

To assess the effect of the textile layer in TRM, various beam models with different numbers of textile layers are established. Four configurations of textile layers, namely 1, 2, 3, and 4 layers, are considered along with two reinforcement methods: TRM alone and TRM combined with integrated steel implants. Additionally, a reference RC beam without TRM treatment (labeled as S_0) is included for comparison. Therefore, a total of nine cases are simulated. The designations for each model in this subsection are provided in Table 2.

Fig. 5a illustrates the predicted load versus mid-span deflection response curves for the nine beam models, while Fig. 5b presents the corresponding load-mid-span rebar strain curves. Fig. 5(c-f) display stress and strain cloud maps at failure for the reinforced RC beams with different textile layers and reinforcement methods. Furthermore, Table 2 summarizes and compares the predicted ultimate load (P_u) and its corresponding mid-span deflection (Δ_u).

From Fig. 5a, it is evident that TRM reinforcement enhances the loading-carrying capacity, resulting in higher P_u, as anticipated. As the number of textile layers increases, the pre-cracking stiffness, post-cracking stiffness, and P_u of the reinforced RC beams exhibit a significant increase. This observation is consistent with the findings reported by Koutas et al. [35]. Moreover, Fig. 5b indicates that an increase in textile layers gradually decreases the strain in the reinforcement steel. This can be attributed to the greater load-sharing capacity of TRM with an increased number of layers. However, Table 2 indicates that TRM reduces the ductility of the beams. Compared to the control beam (S_0), TRM reinforced beams demonstrate considerably lower Δ_u. Interestingly, the ductility of the RC beams reinforced with TRM slightly improves with increasing number of textile layers, whereas the RC beams reinforced with TRM plus integrated steel implants show a slight decrease in ductility.

From Table 2, it can also be observed that the P_u reaches its maximum for both beams when the textile layer number is 4 and is improved by 65.07 % and 61.86 %, respectively, compared to the S_0 group. The lower improvement in strength for S_2-N_4 can be attributed to the stress concentration caused by the integrated steel implants. This is further demonstrated by the failure modes of each group of beams in Fig. 5(c-f). The failure mode of both groups of beams is flexural failure when the number of textile layers is 1–3. Notably, the failure mode of S_1-N_4 is shear failure at the two ends of the TRM, while S_2-N_4 undergoes flexural failure due to high stress concentration in the middle section caused by the integrated steel implants. The shear failure of S_1-N_4 is mainly due to the high TRM stiffness and the premature yielding of the stirrups. Accordingly, it is suggested that the stirrup ratio and the number of textile layers should be rationally adjusted in TRM reinforced RC beams to further improve the flexural performance. Furthermore, the highest number of cracks in the RC beams is observed when the number of textile layer is 4. This may be due to the more uniform stress distribution in the beams caused by the higher stiffness of the TRM. Additionally, the integrated steel implants have no significant effect on the number of cracks in TRM-strengthened RC beams.

5.2. *Longitudinal length of textile*

To evaluate the influence of TRM's longitudinal length of textile, various beam models with different longitudinal lengths of textile were constructed. The four different lengths considered were 1300 mm, 1500 mm, 1700 mm, and 1900 mm. Two reinforced methods, namely TRM and TRM plus integrated steel implants, were employed. For comparison, an unreinforced RC beam (labeled as S_0) was also included, resulting in nine simulated cases. The designations for each model in this subsection are provided in Table 3.

The load–deflection curves for the nine beam models are presented in Fig. 6a, while the corresponding mid-span rebar strain curves are shown

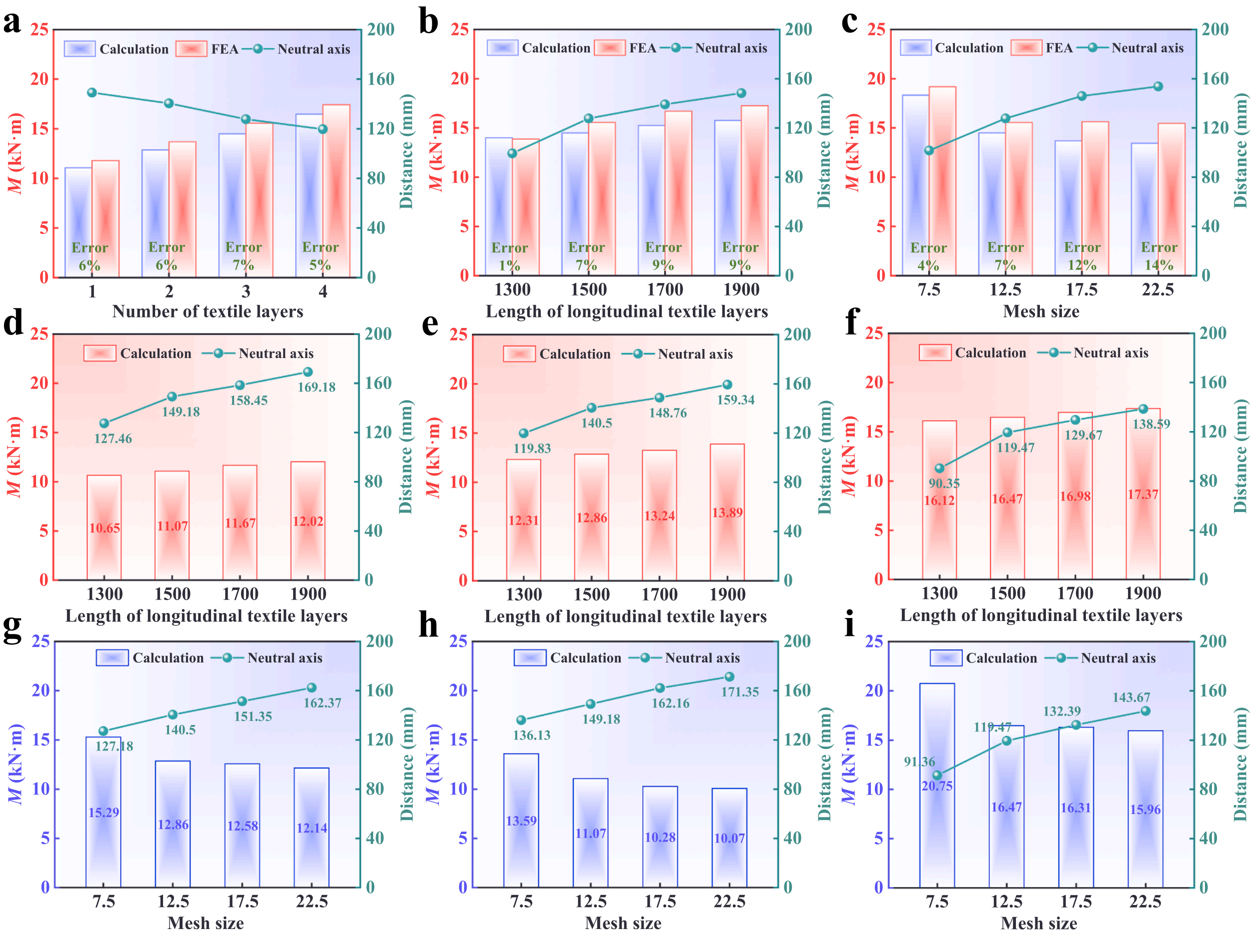

Fig. 9. Comparison of analytical model calculations and FE analysis results: (a) Different number of textile layers; (b) Different textile longitudinal lengths; (c) Different textile mesh sizes. Predicted results of TRM-strengthened RC beams for different textile longitudinal lengths: (d) 1 textile layer; (e) 2 textile layers; (f) 4 textile layers. Predicted results of TRM reinforced RC beams for different textile mesh sizes: (g) 1 textile layer; (h) 2 textile layers; (i) 4 textile layers.

in Fig. 6b. The stress and strain cloud maps at failure for reinforced RC beams with different longitudinal lengths of textile and reinforced methods are displayed in Fig. 6(c-f). Additionally, Table 3 summarizes and compares the P_u and its corresponding Δ_u.

Similar to the textile layers, it can be found from Fig. 6a and Table 3 that regardless of the length of textile, TRM reinforcement increases the loading-carry capacity but lower the ductility of RC beams. The strain of the reinforcement steel is observed to increase gradually with an increase in the longitudinal length of the textile for RC beams reinforced by TRM in the tensile area, as shown in Fig. 6b. However, no such trend is observed for RC beams reinforced by TRM plus integrated steel implants. From Table 3, it can also be observed that the P_u reaches its maximum for both beam types when the textile longitudinal length is 1900 mm, with improvement of 63.55 % and 58.01 %, respectively, compared to the S_0 group. The slightly lower improvement in S_2-L_{1900} compared to S_1-L_{1900} is attributed to the stress concentration effect caused by the integrated steel implants, similar to the results observed with varying textile layers.

It can be noticed from Fig. 6(c-f) that the failure mode of both beams is shear failure when the textile longitudinal length is 1300 mm. For cases with longer textile longitudinal lengths, the failure mode is flexural failure. Shear failure at shorter textile lengths is primarily due to the TRM being too short to fully sustain the tensile strain at the bottom of the beam and the sudden change in stiffness at the TRM end position. These factors result in large shear stress at the TRM's end, leading to shear failure. Conversely, when the TRM length is sufficient, it can share most of the tensile stress at the bottom of the beam until the textile breaks, resulting in flexural failure. Notably, integrated steel implants reduce the number of cracks in TRM-strengthened RC beams with a textile length of 1300 mm, but have no significant effect on beams with other textile lengths. This phenomenon may be related to the integrated steel implants having a more substantial effect on the stress distribution within the TRM when the textile length is 1300 mm.

5.3. Textile mesh size

To examine the impact of the textile mesh size in TRM, beam models with different mesh sizes were constructed. Four different mesh sizes were considered: 7.5 mm × 7.5 mm, 12.5 mm × 12.5 mm, 17.5 mm × 17.5 mm, and 22.5 mm × 22.5 mm. Two reinforcement methods, TRM and TRM plus integrated steel implants, were employed. A smaller mesh size indicates a denser mesh. Additionally, an unreinforced RC beam (labeled as S_0) was included for comparison , resulting in a total of nine cases. The designations for each model in this subsection are provided in Table 4.

Fig. 7a shows the load–deflection response curves for the nine beam models. Fig. 7b presents the corresponding mid-span rebar strain curves. The stress and strain cloud maps at failure for reinforced RC beams with different mesh sizes and reinforcement methods are displayed in Fig. 7 (c-f). Furthermore, Table 4 summarizes and compares the P_u and its corresponding Δ_u.

From Fig. 7a and Table 4, it is clear that TRM-strengthened RC beams with different mesh sizes have higher P_u but lower ductility than the control beam (S_0). However, differing from the above findings, the P_u of the TRM-strengthened RC beams remains relatively stable while ductility gradually increases as the mesh size exceeds 7.5 mm × 7.5 mm. Fig. 7a also illustrates that the stiffness of the TRM-strengthened RC beams decreases both before and after cracking as the textile mesh size increases. Fig. 7b shows that flexural steel strain gradually increases with the increasing mesh size, indicating a decreasing bearing capacity of TRM. From Table 4, it can also be found that the P_u reaches its maximum for both beams when the textile longitudinal length is 7.5 mm × 7.5 mm, with improvements of 81.79 % and 82.22 %, respectively, compared to the S_0 group. Notably, integrated steel implants enhance the strengthening effect of TRM-strengthened RC beams with mesh sizes of 7.5 mm × 7.5 mm, 12.5 mm × 12.5 mm, and 22.5 mm × 22.5 mm. This phenomenon may be related to the positioning of the textile within the TRM.

Fig. 7(c-f) show that when the mesh sizes are 7.5 mm × 7.5 mm and 17.5 mm × 17.5 mm, the failure mode of beams is shear failure. Moreover, the shear failure morphology indicates that the concrete rips at the end of the TRM, followed by a shear inclined crack emerging from within the TRM due to the stirrup yielding. This may be related to the higher stiffness of the TRM and the positional distribution of the textile. When the textile mesh sizes are 12.5 mm × 12.5 mm and 22.5 mm × 22.5 mm, the failure mode shifts to flexural failure. Additionally, for a mesh size of 22.5 mm × 22.5 mm, the presence of integrated steel implants alters the bending failure mode of TRM-strengthened RC beams from a single fracture to two symmetrical fractures (see Fig. 7(c-f)). Furthermore, the highest number of cracks in TRM-strengthened RC beams is observed with a mesh size of 7.5 mm × 7.5 mm. These results indicate that the mesh size significantly affects the flexural performance, failure mode and effect of integrated steel implants in TRM reinforced RC beams. However, the detailed mechanism behind the mesh size effect needs further exploration in subsequent studies.

6. Analytical model for predicting flexural strength of TRM-strengthened RC beams

This section proposes an analytical model to calculate the flexural strength of TRM-strengthened RC beams. The derivation of the model is explained, and the predicted results FE modelling outcomes.

Considering that TRM-strengthened RC beams exhibit similarities with FRP-reinforced RC beams in terms of flexural performance [17], the flexural strength of TRM-strengthened RC beams can be predicted using a similar analytical method. According to the Chinese standard GB 50608–2010 [68], the area division and force balance of the beam cross-section under bending are illustrated in Fig. 8. The flexural strength can be derived and expressed as follows:

$$M = f_y'A_s'(\frac{\boldsymbol{h}}{2}-x_1-a')+\int_{x_2}^{h/2-x_1}\omega f_c\boldsymbol{b}xdx+f_yA_s(\frac{\boldsymbol{h}}{2}+x_1-a)+\sigma_{fd}A_f(\frac{\boldsymbol{h}}{2}+x_1+\frac{\boldsymbol{t}}{2}) \tag{26}$$

$$\int_{x_2}^{h/2-x_1}\omega f_c\mathrm{b}dx+f_y'A_s' = f_yA_s+\sigma_{fd}A_f \tag{27}$$

$$\sigma_{fd} = \boldsymbol{min}\left\{f_{fd}, E_f\varepsilon_{fe,m1}, E_f\varepsilon_{fe,m2}\right\} \tag{28}$$

where M is the bending moment when the TRM-strengthened RC beam reaches ultimate load capacity; b and h are the width and height of the beam section; t is the thickness of the TRM, which in this study is taken as 5 mm, 10 mm, 18 mm and 20 mm respectively depending on the number of textile layers; x is the height of the concrete in the compression zone when the TRM-strengthened RC beam reaches ultimate load; x_1 is the distance from the neutral axis to the center of the beam when the TRM-strengthened RC beam reaches ultimate load; x_2 is the distance from the yield surface to the neutral axis when the TRM-strengthened RC beam reaches ultimate load, and in this paragraph it is assumed that concrete is not loaded; a and a' are the distances from the centre of the section of the tensile and compressive bars to the top and bottom edges of the concrete respectively; A_s and A_s' are the cross-sectional areas of the tensile and compressive bars respectively; f_c is the design value of the axial compressive strength of the concrete; f_y and f_y' are the design values of the tensile and compressive strengths of the tensile and compressive bars, respectively; σ_{fd}, A_f, E_f and f_{fd} are the stress, cross-sectional area, modulus of elasticity and ultimate tensile strength of the equivalent carbon fiber bundle respectively ; $\varepsilon_{fe,m1}$ and $\varepsilon_{fe,m2}$ are the effective strains of the FRP when the compression zone of concrete reaches the ultimate compressive strain or FRP de-bond from the concrete substrate, respectively. The equivalent force reduction factor ω can be calculated using Eq. (29) and A_f is calculated from Eq. (30) depending on the type of textile arrangement.

$$\omega = \begin{cases} 0.5+0.5\frac{\varepsilon_{fe,m2}}{\varepsilon_{fc,m1}}\left(\varepsilon_{fe,m1} > \varepsilon_{fc,m2}\right) \\ 0.5+0.5\frac{f_{fd}/E_f}{\varepsilon_{fc,m1}}\left(E_f\varepsilon_{fe,m1} > f_{fd}\right) \end{cases} \tag{29}$$

$$A_f = \frac{nm\pi r^2}{4} \tag{30}$$

where n is the number of textile layers, m is the number of equivalent carbon fiber bundles in a layer and r is the equivalent carbon fiber bundle diameter (here taken as 0.757 mm). It should be particularly noted that in the above Eqs. (26–30) calculations, the equivalent form center of the textile is taken to be at the center of the TRM.

The ultimate flexural strength of TRM-strengthened RC beams was predicted using Eqs. (25–29). The predicted results were compared with the FE analysis results, as shown in Table 5 and Fig. 9(a-c). The calculated flexural strength of TRM-strengthened RC beams using the analytical model closely matches the FE analysis results, with an error of less than 15 %. Fig. 9a shows that ultimate flexural strength increases with the number of textile layers, and the neutral axis consistently shifts downward, indicating increased stiffness in the beam's lower part. Fig. 9b reveals that as textile length increases, ultimate flexural strength also increases, with an upward shift in the neutral axis, indicating improved ductility. However, when the mesh size exceeds 17.5 mm × 17.5 mm, ultimate flexural strength stabilizes while the neutral axis position continues to rise (Fig. 9c). The predicted results for larger mesh sizes show significant deviations from the FE analysis results, suggesting that while larger mesh sizes do not impact ultimate load capacity, they significantly influence ductility. Further investigation is needed to understand these variations. Overall, the proposed analytical model effectively predicts the ultimate flexural strength of TRM-strengthened RC beams under different textile parameters, as confirmed by the consistency with FE analysis results.

The analytical model was also used to predict the M_u and x for TRC-strengthened RC beams without integrated steel implants, considering the textile layers of 1, 2 and 4. The results are presented in Fig. 9(d-i). Here the textile longitudinal length and mesh size parameters of TRM-strengthened RC beams are same as above mentioned study. It can be observed that the trends of M_u and x of TRM-strengthened RC beams with the three textile layers agree with the above calculated results, confirming the model's reliability under different textile parameters.

7. Findings and conclusions

In this study, a numerical model of TRM-strengthened RC beams was proposed and validated. The developed FE model was extended to facilitate the numerical design of TRM-strengthened RC beams by assessing various parameters, including the number of textile layers, textile length, and textile mesh size. Additionally, an analytical model was derived to enable rapid prediction of the flexural strength of TRM-strengthened RC beams. Based on the obtained results, the following findings can be summarized:

1. The established FE model effectively simulated the flexural behavior and failure mode of TRM-strengthened RC beams, demonstrating good agreement with experimental results.
2. Compared to RC beams, TRM-strengthened RC beams, including those with integrated steel implants, exhibited higher flexural strength and lower ductility.
3. Increasing the number of textile layers significantly enhanced the pre-cracking stiffness, post-cracking stiffness, and flexural capacity of TRM-strengthened RC beams, while ductility decreased gradually. The integrated steel implants slightly reduced the improvement in ultimate bearing capacity of TRM-strengthened RC beams compared to beams without integrated steel implants, except for 3 textile layers.
4. The longitudinal length of the textile had a positive effect on the ultimate flexural strength and ductility of TRM-strengthened RC beams. Thus, appropriate textile length can be selected based on the desired load capacity and ductility requirements
5. The flexural load capacity of TRM-strengthened RC beams showed minimal change when the textile mesh size exceeded 17.5 mm × 17.5 mm, while the ductility gradually increased. Consequently, it is recommended to use a textile mesh size of 17.5 mm × 17.5 mm in practical engineering applications.
6. The proposed analytical models reasonably predicted the flexural strength of TRM-strengthened RC beams, with prediction accuracies all above 0.85

However, since the members of the FE model developed in this study were in perfect contact with each other, this prevented the premature failure phenomenon that might occur in the test from appearing in the simulation results. In future studies, the contact between textile and mortar as well as between TRM and RC beams in the FE model will be adjusted to better reproduce the premature failure phenomenon.

CRediT authorship contribution statement

Peng Cao: Conceptualization, Formal analysis, Funding acquisition, Investigation, Methodology, Writing – original draft. **Liang Cao:** Data curation, Formal analysis, Investigation, Visualization, Writing – original draft. **Guoqing Chen:** Methodology, Writing – review & editing. **Zhengdong Zhi:** Data curation, Formal analysis, Investigation. **Jianru Wang:** Data curation, Formal analysis, Investigation. **Zhidan Yuan:** Data curation, Methodology, Software, Validation. **Zhifei Tan:** Investigation, Supervision, Writing – review & editing.

Declaration of competing interest

The authors declare that they have no known competing financial interests or personal relationships that could have appeared to influence the work reported in this paper.

Data availability

Data will be made available on request.

Acknowledgements

This work was financially supported by the National Natural Science Foundation of China (51769028, 51508137). All the sources of support are gratefully acknowledged. Any opinions, findings, and conclusions or recommendations expressed in this paper are those of the authors and do not necessarily reflect the views of the sponsors.

References

[1] A.T. Baraghith, W. Mansour, R.N. Behiry, S. Fayed, Effectiveness of SHCC strips reinforced with glass fiber textile mesh layers for shear strengthening of RC beams: Experimental and numerical assessments, Constr. Build. Mater. 327 (2022) 127036.
[2] R.A. Hawileh, H.A. Musto, J.A. Abdalla, M.Z. Naser, Finite element modeling of reinforced concrete beams externally strengthened in flexure with side-bonded FRP laminates, Compos. B. Eng. 173 (2019) 106952.
[3] R.A. Hawileh, H.H. Mhanna, A.A. Rashed, J.A. Abdalla, M.Z. Naser, Flexural behavior of RC beams externally bonded with polyethylene terephthalate (PET) fiber reinforced polymer (FRP) laminates, Eng. Struct. 256 (2022) 114036.
[4] K. Douier, R. Hawileh, J.A. Abdalla, N.A. Nuaimi, M.G. Sohail, Durability performance of RC beams strengthened with CFRP laminates and galvanized steel mesh bonded with epoxy and mortar systems, Structures. 55 (2023) 338–353.
[5] S. Cheng, S. Yin, L. Jing, Comparative experimental analysis on the in-plane shear performance of brick masonry walls strengthened with different fiber reinforced materials, Constr. Build. Mater. 259 (2020) 120387.
[6] F. Qin, X. Wei, Y. Lu, Z. Zhang, J. Di, Z. Yin, Flexural behaviour of high strength engineered cementitious composites (ECC)-reinforced concrete composite beams, Case Stud. Constr. Mater. 18 (2023) e02002.
[7] M. Zhang, M. Deng, Tensile behavior of textile-reinforced composites made of highly ductile fiber-reinforced concrete and carbon textiles, J. Build. Eng. 57 (2022) 104824.
[8] Y. Elmezayen, T. El-Maaddawy, Restoration of two-span RC beams with severely corroded reinforcement using C-FRCM composites, Structures. 63 (2024) 106331.
[9] O. Awani, T. El-Maaddawy, N. Ismail, Fabric-reinforced cementitious matrix: A promising strengthening technique for concrete structures, Constr. Build. Mater. 132 (2017) 94–111.
[10] S.D. Santis, P. Casadei, G.D. Canio, G.D. Felice, M. Malena, M. Mongelli, I. Roselli, Seismic performance of masonry walls retrofitted with steel reinforced grout, Earthq. Eng. Struct. Dyn. 45 (2) (2015) 229e51.
[11] G.D. Canio, G.D. Felice, S.D. Santis, A. Giocoli, M. Mongelli, F. Paolacci, I. Roselli, Passive 3D motion optical data in shaking table tests of a SRG-reinforced masonry wall, Earthq. Struct. 10 (1) (2016) 53–71.
[12] P. Rawat, S. Liu, S. Guo, M.Z. Rahman, T. Yang, X. Bai, Y. Yao, B. Mobasher, D. Zhu, A state-of-the-art review on mechanical performance characterization and modelling of high-performance textile reinforced concretes, Constr. Build. Mater. 347 (2022) 128521.
[13] A.S.M.A. Awal, H. Mohammadhosseini, Green concrete production incorporating waste carpet fiber and palm oil fuel ash, J. Clean. Prod. 137 (2016) 157–166.
[14] M. Kurban, O. Babaarslan, İ.H. Çağatay, Investigation of the flexural behavior of textile reinforced concrete with braiding yarn structure, Constr. Build. Mater. 334 (2022) 127434.
[15] Y. Qin, Y. Li, X. Zhang, H. Zhou, Constitutive model of polypropylene-fiber-fabric-reinforced concrete under uniaxial compression and index conversion of mechanical properties, Constr. Build. Mater. 347 (2022) 128508.
[16] P. Peña-Pichardo, G. Martínez-Barrera, M. Martínez-López, F. Ureña-Núñez, J.M.L. d. Reis,, Recovery of cotton fibers from waste Blue-Jeans and its use in polyester concrete, Constr. Build. Mater. 177 (2018) 409–416.
[17] H. Zhang, H. Liu, V. Kodur, M. Li, Y. Zhou, Flexural behavior of concrete slabs strengthened with textile reinforced geopolymer mortar, Compos. Struct. 284 (2022) 115220.
[18] Y. Al-Salloum, H.M. Elsanadedy, S. Alsayed, R. Iqbal, Experimental and Numerical Study for the Shear Strengthening of Reinforced Concrete Beams Using Textile-Reinforced Mortar, J. Compos. Constr. 16 (1) (2012) 74–90.
[19] K. Junaid, M. Zyed, A. Nonna, G. Cai, S.L. Amir, Tensile and cracking behaviour of crimped textile reinforced mortar (TRM) based on digital image correlation, Constr. Build. Mater. 417 (2024) 135321.
[20] P. Yang, T. Krevaikas, Experimental and analytical investigation of the tensile mechanism of textile-reinforced mortar (TRM) composites and fabric grids in elevated temperatures, Constr. Build. Mater. 431 (2024) 136459.
[21] S.D. Santis, F.G. Carozzi, G.D. Felice, C. Poggi, Test methods for Textile Reinforced Mortar systems, Compos. B. Eng. 127 (2017) 121–132.
[22] L. Estevan, F.B. Varona, F.J. Baeza, B. Torres, D. Bru, Textile Reinforced Mortars (TRM) tensile behavior after high temperature exposure, Constr. Build. Mater. 328 (2022) 127116.
[23] H.H. Pham, N.H. Dinh, S.-H. Kim, S.-H. Park, K.-K. Choi, Tensile behavioral characteristics of lightweight carbon textile-reinforced cementitious composites, J. Build. Eng. 57 (2022) 104848.
[24] A. Chira, A. Kumar, T. Vlach, L. Laiblová, A.S. Škapin, P. Hájek, Property improvements of alkali resistant glass fibres/epoxy composite with nanosilica for textile reinforced concrete applications, Mater. Des. 89 (2016) 146–155.
[25] E.I. Saqan, H.A. Rasheed, T. Alkhrdaji, Evaluation of the seismic performance of reinforced concrete frames strengthened with CFRP fabric and NSM bars, Compos. Struct. 184 (2018) 839–847.
[26] J.A. Abdalla, H.H. Mhanna, A.r B. Ali, R. A. Hawileh,, CFRP U-Wraps and Spike Anchors for Enhancing the Flexural Performance of CFRP-Plated RC Beams, Polymers 15 (7) (2023) 1621.
[27] M. Assad, R.A. Hawileh, J.A. Abdalla, Flexural strengthening of reinforced concrete beams with CFRP laminates and spike anchors, Composites Part C: Open Access 13 (2024) 100443.
[28] S. Cholostiakow, Z. Ren, I. Skyrianou, L. Koutas, C. Papakonstantinou, E. Bescher, T. Hanein, Bond of textile-reinforced belite calcium sulfoaluminate cement mortar to concrete substrate, Mater. Struct. 57 (2024) 82.

[29] Y.M. Alharthi, M. Emara, A.S. Elamary, I.A. Sharakyad, Flexural response and load capacity of reinforced concrete beams strengthened with reinforced mortar layer, Eng. Struct. 245 (2021) 112884.

[30] A. Brückner, R. Ortlepp, M. Curbach, Anchoring of shear strengthening for T-beams made of textile reinforced concrete (TRC), Mater. Struct. 41 (2) (2008) 407–418.

[31] A.C.H. Giese, D.N. Giese, V.F.P. Dutra, L.C.P.D.S. Filhoc, Flexural behavior of reinforced concrete beams strengthened with textile reinforced mortar, J. Build. Eng. 33 (2021) 101873.

[32] L.N. Koutas, C.G. Papakonstantinou, Flexural strengthening of RC beams with textile-reinforced mortar composites focusing on the influence of the mortar type, Eng. Struct. 246 (2021) 113060.

[33] N. Revanna, C.K.S. Moy, Experimental study on reinforced concrete beams strengthened with Basalt and Carbon Textile Reinforced mortars at elevated temperatures, Eng. Struct. 307 (2024) 117921.

[34] S. Song, M. Deng, Y. Zhang, Effects of textile type on the flexural properties of prefabricated hollow-core slabs strengthened with PVA fibers-improved TRM, J. Build. Eng. 87 (2024) 109103.

[35] L.N. Koutas, D.A. Bournas, Flexural Strengthening of Two-Way RC Slabs with Textile-Reinforced Mortar: Experimental Investigation and Design Equations, J. Compos. Constr. 21 (1) (2017) 04016065.

[36] C.T.N. Tran, X.H. Nguyen, A.T. Le, H.C. Nguyen, D.D. Le, Shear tests of GFRP-reinforced concrete beams strengthened in shear by textile reinforced concrete, Structures 34 (2021) 4339–4349.

[37] Z.C. Tetta, L.N. Koutas, D.A. Bournas, Textile-reinforced mortar (TRM) versus fiber-reinforced polymers (FRP) in shear strengthening of concrete beams, Compos. B. Eng. 77 (2015) 338–348.

[38] L. Guo, M. Deng, H. Chen, R. Li, X. Ma, Y. Zhang, Experimental study on pre-damaged RC beams shear-strengthened with textile-reinforced mortar (TRM), Eng. Struct. 256 (2022) 113956.

[39] N.H. Dinh, S.-H. Park, S.-H. Kim, K.-K. Choi, Cyclic behavioral characteristics of RC beams strengthened by U-wrapped TRM jacket with anchorage details, Eng. Struct. 247 (2021) 113205.

[40] S.H. Park, N.H. Dinh, J.W. Um, K.K. Choi, Experimental study on the seismic performance of RC columns retrofitted by lap-spliced textile-reinforced mortar jackets after high-temperature exposure, Compos. Struct. 256 (2021) 113108.

[41] L. Guo, M. Deng, T. Li, Seismic behaviour of RC columns retrofitted with textile-reinforced mortar (TRM) optimized by short PVA fibres, Structures 50 (2023) 244–254.

[42] P. Colajanni, F.D. Domenico, A. Recupero, N. Spinella, Concrete columns confined with fibre reinforced cementitious mortars: Experimentation and modelling, Constr. Build. Mater. 52 (2014) 375–384.

[43] F. Faleschini, M.A. Zanini, L. Hofer, C. Pellegrino, Experimental behavior of reinforced concrete columns confined with carbon-FRCM composites, Constr. Build. Mater. 243 (2020) 118296.

[44] Q. Zhang, Z.-Y. Wei, X.-L. Gu, Q.-C. Yang, S.-Y. Li, Y.-S. Zhao, Confinement behavior and stress–strain response of square concrete columns strengthened with carbon textile reinforced concrete (CTRC) composites, Eng. Struct. 266 (2022) 114592.

[45] L. Ombres, Flexural analysis of reinforced concrete beams strengthened with a cement based high strength composite material, Compos. Struct. 94 (1) (2011) 143–155.

[46] S. Song, M. Deng, M. Zhang, L. Guo, Z. Dong, P. Li, Flexural strengthening of reinforced concrete beams using textile-reinforced mortar improved with short PVA fibers, Structures 56 (2023) 104824.

[47] H.M. Elsanadedy, T.H. Almusallam, S.H. Alsayed, Y.A. Al-Salloum, Flexural strengthening of RC beams using textile reinforced mortar – Experimental and numerical study, Compos. Struct. 97 (2013) 40–55.

[48] U. Ebead, K.C. Shrestha, M.S. Afzal, A.E. Refai, Effectiveness of fabric-reinforced cementitious matrix in strengthening reinforced concrete beams, J. Compos. Constr. 21 (2) (2017) 04016084.

[49] A. D'Ambrisi, F. Focacci, Flexural strengthening of RC beams with cement-based composites, J. Compos. Constr. 15 (5) (2011) 707–720.

[50] S.M. Raoof, L.N. Koutas, D.A. Bournas, Textile-reinforced mortar (TRM) versus fibre-reinforced polymers (FRP) in flexural strengthening of RC beams, Constr. Build. Mater. 151 (2017) 279–291.

[51] F. Schladitz, M. Frenzel, D. Ehlig, M. Curbach, Bending load capacity of reinforced concrete slabs strengthened with textile reinforced concrete, Eng. Struct. 40 (2012) 317–326.

[52] N.W. Portal, L.N. Thrane, K. Lundgren, Flexural behaviour of textile reinforced concrete composites: experimental and numerical evaluation, Mater. Struct. 50 (2017) 4.

[53] I.G. Colombo, M. Colombo, M. Prisco, F. Pouyaei, Analytical and numerical prediction of the bending behaviour of textile reinforced concrete sandwich beams, J. Build. Eng. 17 (2018) 183–195.

[54] A. Parvin, M. Alhusban, Finite-Element Analysis of Textile-Reinforced Mortar Strengthening of Shear-Deficient Reinforced Concrete Beams, J. Compos. Constr. 26 (2022) 04022037.

[55] J. Donnini, V. Corinaldesi, A. Nanni, Mechanical properties of FRCM using carbon fabrics with different coating treatments, Compos. B. Eng. 88 (2016) 220.

[56] S. Guo, J. Ren, T. Yang, M.Z. Rahman, C. Shi, D. Zhu, Influences of surface treatment on the mechanical performances of carbon and basalt textiles-reinforced concretes under harsh environments, Compos. B. Eng. 246 (2022) 110195.

[57] GB/T 3362-2017. Test methods for tensile properties of carbon fiber multifilament, Beijing: Standards Press of China; 2017 (in Chinese).

[58] S. Feng, H. Xiao, J. Geng, Bond strength between concrete substrate and repair mortar: Effect of fibre stiffness and substrate surface roughness, Cem Concr Compos. 114 (2020) 103746.

[59] Y.D. Murray, User's manual for LS-DYNA concrete material model 159. Report no. FHWA-HRT-05-062. USA: US Department of Transportation, Federal Highway Administration National Transportation Systems Center (2007).

[60] Y.D. Murray, A. Abu-Odeh, R. Bligh, Evaluation of concrete material model 159. Report no. FHWA-HRT-05-063. USA: US Department of Transportation, Federal Highway Administration National Transportation Systems Center (2007).

[61] T.J.R. Hughes, W.K. Liu, Nonlinear finite element analysis of shells-part II. two-dimensional shells, Comput. Methods Appl. Mech. Eng. 27 (1981) 167–181.

[62] F. Tschuchnigg, H.F. Schweiger, The embedded pile concept – Verification of an efficient tool for modelling complex deep foundations, Comput. Geotech. 63 (2014) 244–254.

[63] M.L. Benzeggagh, M. Kenane, Measurement of mixed-mode delamination fracture toughness of unidirectional glass/epoxy composites with mixed-mode bending apparatus, Compos. Sci. Technol. 56 (4) (1996) 439–449.

[64] P. Larrinaga, L. Garmendia, C. Chastre, J.-T. San-José, Low-grade RC beams strengthened with TRM composite based on basalt, carbon and steel textiles: Experimental and analytical study, Case Stud. Constr. Mater. 16 (2022) e00906.

[65] M. Halvaei, M. Jamshidi, M. Latifi, M. Ejtemaei, Experimental investigation and modelling of flexural properties of carbon textile reinforced concrete, Constr. Build. Mater. 262 (2020) 120877.

[66] H. Kim, Y. You, G. Ryu, Flexural Strengthening of RC Slabs with Lap-Spliced Carbon Textile Grids and Cementitious Grout, Materials 15 (8) (2022) 2849.

[67] Y.X. Du, X. Shao, S.H. Chu, F. Zhou, R.K.L. Su, Strengthening of preloaded RC beams using prestressed carbon textile reinforced mortar plates, Structures 30 (2021) 735–744.

[68] GB 50608-2010. Technical code for infrastructure application of FRP composites. Beijing: China Planning Press; 2011 (in Chinses).